Orienting Ocean-Bottom Seismometers from P-wave and Rayleigh wave polarizations

J.-R Scholz, Guilhem Barruol, Fabrice R. R. Fontaine, Karin Sigloch, Wayne C. Crawford, Martha Deen

Geophysical Journal International

Geophys. J. Int. (2017) **208,** 1277–1289
Advance Access publication 2016 November 10
GJI Seismology

doi: 10.1093/gji/ggw426

Orienting ocean-bottom seismometers from *P*-wave and Rayleigh wave polarizations

John-Robert Scholz,[1] Guilhem Barruol,[1] Fabrice R. Fontaine,[1] Karin Sigloch,[2] Wayne C. Crawford[3] and Martha Deen[3]

[1] *Laboratoire GéoSciences Réunion, Université de La Réunion, Institut de Physique du Globe de Paris, Sorbonne Paris Cité, UMR* 7154 *CNRS, F-*97744 *Saint Denis, France. E-mail: scholz@ipgp.fr*
[2] *Department of Earth Sciences, University of Oxford, South Parks Road, Oxford OX1* 3*AN, United Kingdom*
[3] *Institut de Physique du Globe de Paris, Sorbonne Paris Cité, Université Paris Diderot, UMR* 7154 *CNRS, F-*75238 *Paris, France*

Accepted 2016 November 8. Received 2016 November 3; in original form 2016 June 14

SUMMARY

We present two independent, automated methods for estimating the absolute horizontal misorientation of seismic sensors. We apply both methods to 44 free-fall ocean-bottom seismometers (OBSs) of the RHUM-RUM experiment (http://www.rhum-rum.net/). The techniques measure the 3-D directions of particle motion of (1) *P*-waves and (2) Rayleigh waves of earthquake recordings. For *P*-waves, we used a principal component analysis to determine the directions of particle motions (polarizations) in multiple frequency passbands. We correct for polarization deviations due to seismic anisotropy and dipping discontinuities using a simple fit equation, which yields significantly more accurate OBS orientations. For Rayleigh waves, we evaluated the degree of elliptical polarization in the vertical plane in the time and frequency domain. The results obtained for the RHUM-RUM OBS stations differed, on average, by 3.1° and 3.7° between the methods, using circular mean and median statistics, which is within the methods' estimate uncertainties. Using *P*-waves, we obtained orientation estimates for 31 ocean-bottom seismometers with an average uncertainty (95 per cent confidence interval) of 11° per station. For 7 of these OBS, data coverage was sufficient to correct polarization measurements for underlying seismic anisotropy and dipping discontinuities, improving their average orientation uncertainty from 11° to 6° per station. Using Rayleigh waves, we obtained misorientation estimates for 40 OBS, with an average uncertainty of 16° per station. The good agreement of results obtained using the two methods indicates that they should also be useful for detecting misorientations of terrestrial seismic stations.

Key words: Broad-band seismometers; Body waves; Surface waves and free oscillations; Seismic anisotropy; Seismic instruments; Indian Ocean.

1 INTRODUCTION

Ocean-bottom seismometer (OBS) technology has greatly evolved over the past few decades, opening new pathways to investigating crustal and mantle structures through passive seismic experiments. Major improvements have been made in several complementary directions: (i) power consumption, data storage and battery energy density, allowing deployments with continuous recordings for more than one year, (ii) design of levelling and release systems, allowing high recovery rates (>99 per cent) and good instrument levelling, and (iii) seismometer design, permitting the reliable deployment of true broad-band sensors to the ocean floor.

Such advances enable long-term, high-quality seismological experiments in the oceans, but there is still no reliable, affordable system to measure horizontal seismometer orientations at the seafloor. Many seismological methods require accurate sensor orientation, including receiver function analyses, SKS splitting measurements and waveform tomography. Accurate orientations are also required in environmental seismology and bioacoustics, e.g., for tracking storms, noise sources or whales. Upon deployment, OBSs are generally released at the sea surface above their targeted landing spots and sink freely to the seafloor. Soon after a seismometer lands, its levelling mechanism activates to align the vertical component with the gravitational field, but the azimuthal orientations of the two horizontal components remain unknown. The lack of measurement of horizontal sensor orientations necessitates *a posteriori* estimates of orientation directions, which are the focus of the present study.

Various sensor orientation methods have been published, using full waveforms, *P*-waves and Rayleigh waves of natural and artificial

sources, and ambient seismic noise (e.g., Anderson *et al*. 1987; Laske 1995; Schulte-Pelkum *et al*. 2001; Ekstrom & Busby 2008; Niu & Li 2011; Grigoli *et al*. 2012; Stachnik *et al*. 2012; Zha *et al*. 2013; Wang *et al*. 2016), although it is not always clear from the literature which experiment used which method and what level of accuracy was obtained. One of the most successful techniques for OBS involves active sources to generate seismic signals with known directions (e.g. Anderson *et al*. 1987) but this requires specific equipment and ship time, often combined with time-consuming acoustic triangulation surveys. For the RHUM-RUM deployment, no such active source survey was available.

Our motivation for developing the two presented algorithms was to obtain an orientation procedure which: (i) yields absolute sensor orientations; (ii) works for oceanic and terrestrial sites; (iii) delivers also robust results for temporary networks; (iv) requires no dedicated equipment or expensive, time-consuming measurements (e.g. air guns and/or triangulation); (v) is independent of inter-station distances; (vi) requires no synthetic waveforms or precise event source parameters; (vii) assesses estimates in the time and frequency domain to obtain maximum information; (viii) comes at reasonable computational cost; and (ix) can potentially quantify the influence of seismic anisotropy.

We chose to apply two independent orientation methods which both rely on recordings of teleseismic and regional earthquakes. The first – hereafter called *P-pol* – uses particle motion directions (polarizations) of *P*-waves and is derived from principal component analyses of three-component seismograms. Following Schulte-Pelkum *et al*. (2001) and Fontaine *et al*. (2009), these estimates of ground particle motion are improved by correcting for seismic anisotropy and dipping discontinuities beneath the stations. We applied this technique to our data filtered in nine different frequency passbands, all close to the long-period ocean noise notch, allowing the assessment of measured back-azimuths as a function of frequency. We complement P-pol measurements with a second method – hereafter called *R-pol* – based on polarizations of Rayleigh waves. This method estimates the sensor orientation from the elliptical particle motion in the vertical plane, measured in the time and frequency domain (Schimmel & Gallart 2004; Schimmel *et al*. 2011).

2 EXISTING METHODS FOR ESTIMATING SENSOR ORIENTATION

Active sources (i.e. air guns and explosions) have been successfully used to retrieve horizontal orientations of ocean-bottom sensors (e.g. Anderson *et al*. 1987), but are not available for all OBS deployments. The horizontal orientation of seismometers can also be accurately determined using full waveforms recorded by closely located stations (Grigoli *et al*. 2012), but the method requires very similar wavefields recorded by pairs of sensors and a reference station of known orientation. Such conditions are not applicable to large-scale OBS deployments such as the RHUM-RUM experiment.

Laske (1995) used a non-linear inversion to quantify azimuthal misorientations of terrestrial stations by analysing the polarizations of long-period ($\geq$80 s) surface waves. Stachnik *et al*. (2012) oriented OBS stations using Rayleigh waves (period 25–50 s) radiated from earthquakes ($M_w \geq 6.0$), by correlating the Hilbert-transformed radial component with the vertical seismogram at zero lag-time, based on the method of Baker & Stevens (2004). Stachnik *et al*. (2012) complemented the surface wave analysis with body wave measurements by performing azimuthal grid searches that minimized *P*-wave amplitudes on transverse components. Rueda & Mezcua (2015) used the same methods to verify sensor azimuths for the terrestrial Spanish SBNN array.

Using Rayleigh and Love waves, Ekstrom & Busby (2008) determined sensor orientations by correlating waveforms (period 40–250 s) with synthetic three-component seismograms for specific source parameters. Despite their exclusive use of land stations, they could not establish significant correlations with synthetic waveforms for many earthquakes of $M_w > 5.5$. This severely limits the application to ocean-bottom deployments, which are affected by stronger noise and generally deployed for shorter durations than land stations.

Zha *et al*. (2013) presented a method based on ambient noise (period 5–20 s, essentially Rayleigh waves) to orient OBS, by cross-correlating the Green's function cross and diagonal terms between station pairs. The advantage of Rayleigh-wave observations from ambient noise is that they are much more abundant than those from earthquakes, under the condition that the spatial footprint of the OBS array is small enough for Green's functions to emerge from ambient noise correlations. This condition was not met for our deployment, for which most inter-station distances are from 120 to 300 km.

For *P*-waves, Schulte-Pelkum *et al*. (2001) analysed the deviations of wave polarizations (period $\sim$20 s) recorded at terrestrial stations from their expected great circle paths. They found a quantitative expression relating the observed deviations to sensor misorientation, seismic anisotropy and dipping discontinuities beneath the station. Niu & Li (2011) developed an *SNR*-weighted-multi-event approach to minimize the energy on transverse components using *P*-waves from earthquakes ($M_w \geq 5.5$, period 5–50 s) to retrieve the horizontal sensor azimuths for the terrestrial Chinese CEArray. Wang *et al*. (2016) used a 2-D principal component analysis to evaluate *P*-wave particle motions (period 5–50 s) of teleseismic earthquakes ($M_w \geq 5.5$) to determine the sensors' horizontal misorientations for the terrestrial Chinese NECsaids array. Using a bootstrap algorithm, they further argued that 10 or more good *P*-wave polarization measurements (e.g. highly linearized particle motions) are required to obtain confident error bars on misorientation estimates.

3 DATA SET

Data analysed in this study were recorded by the RHUM-RUM experiment (Réunion Hotspot and Upper Mantle – Réunions Unterer Mantel, www.rhum-rum.net), in which 57 OBSs were deployed over an area of 2000 $\times$ 2000 km^2 in October 2012 by the French *R/V Marion Dufresne* (cruise MD192; Barruol *et al*. 2012; Barruol 2014) and recovered in late 2013 by the German *R/V Meteor* (cruise M101; Sigloch 2013). The 57 OBSs were provided by three different instrument pools: 44 and 4 LOBSTER-type instruments from the German DEPAS and GEOMAR pools, respectively, and 9 LCPO2000-BBOBS type instruments from the French INSU-IPGP pool. The 44 DEPAS and 4 GEOMAR OBS were equipped with broad-band hydrophones (HighTech Inc. HT-01 and HT-04-PCA/ULF 100 s) and wideband three-component seismometers (Guralp 60 s or 120 s sensors) recording at 50 Hz or 100 Hz, whereas the 9 INSU-IPGP OBS used differential pressure gauges (passband from 0.002 to 30 Hz) and broad-band three-component seismometers (Nanometrics Trillium 240 s sensors) and recorded at 62.5 sps. 44 of the stations returned useable seismological data (Fig. 1, green stars). A table summarizing the station characteristics is provided in the Supporting Information. Further details

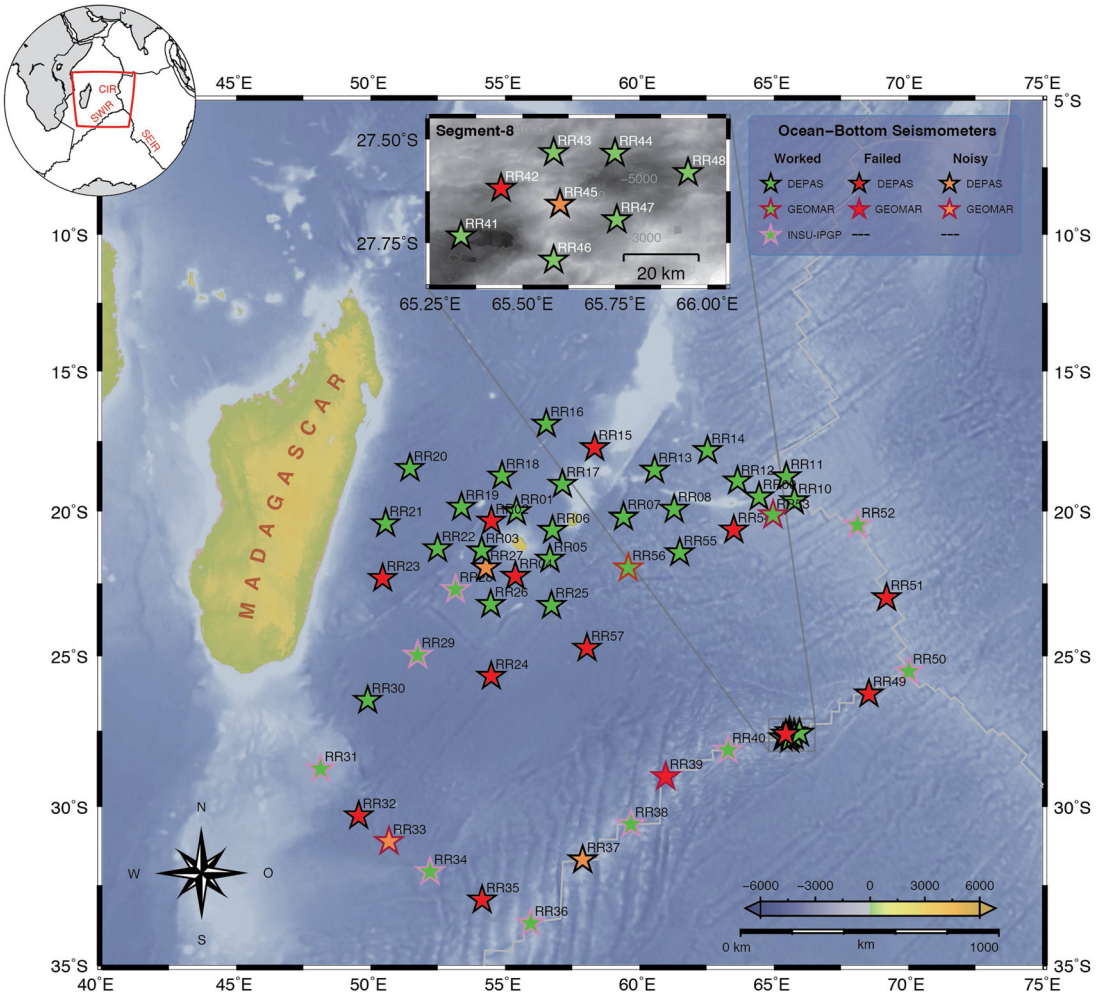

Figure 1. Topography/bathymetry (Amante & Eakins 2009) map of the 57 ocean-bottom seismometers (OBSs) (stars) of the RHUM-RUM network, deployed from October 2012 to December 2013. Fill colour indicates operation status (green = working, red = failed, orange = noisy; Stähler *et al*. 2016). Outline colour indicates OBS type (DEPAS LOBSTER = black, GEOMAR LOBSTER = red, INSU LCPO2000 = pink). OBS were deployed in three circles around La Réunion Island (21.0°S and 55.5°E), along the Southwest Indian Ridge (SWIR), and the Central Indian Ridge (CIR). At SWIR Segment-8, eight densely spaced OBSs were deployed to investigate this ultraslow spreading ridge (Scholz 2014; Schlindwein & Schmid 2016). For OBS deployment depths and positions, see Table S1 in the Supporting Information or Stähler *et al.* (2016).

concerning the network performance, recording periods, data quality, noise levels, and instrumental failures are published in Stähler *et al*. (2016).

4 METHODOLOGY

Throughout this paper, the term '(horizontal) (mis)orientation' of a seismic station refers to the clockwise angle from geographic North to the station's BH1 component, with BH1 oriented 90° anticlockwise to the second horizontal OBS component, BH2 (Fig. 2).

Our two orientation methods are based on the analyses of the 3-D particle motion of *P*-waves (P-pol) and Rayleigh waves (R-pol) of teleseismic and regional earthquakes. Both methods are independent and can be applied to the same seismic event, such as shown for the $M_w = 7.7$ Iran earthquake of 2013 April 16 in Figs 3 (P-pol) and 4 (R-pol). For each technique, a measurement on a single seismogram yields the apparent back-azimuth BAZ_{meas} of the earthquake-station pair, from which we calculated the OBS orientation (*orient*) in degrees as

$$orient = (BAZ_{expec} - BAZ_{meas} + 360^\circ) \bmod 360^\circ, \quad (1)$$

where mod denotes the modulo operator. The expected back-azimuth BAZ_{expec} is the clockwise angle at the station from geographic North to the great circle path linking source and receiver (Fig. 2). The measured, apparent back-azimuth BAZ_{meas} is the clockwise angle from the station's BH1 component to the direction of maximum particle motion (Fig. 2).

4.1 Polarization of regional and teleseismic *P*-waves (P-pol)

In the absence of anisotropy and dipping discontinuities beneath seismic stations, *P*-waves are radially polarized and the associated particle motion is contained along the seismic ray. For geographically well-oriented seismic stations (BH1 aligned with geographic North), BAZ_{meas} should therefore coincide with BAZ_{expec}. There is a 180° ambiguity in BAZ_{meas} if BAZ_{expec} is unknown (Fig. 2).

Seismic anisotropy, however, affects *P*-wave polarizations so that they may deviate from their theoretical back-azimuths. An individual *P*-wave polarization measurement therefore potentially contains the effects of both the station misorientation and the sub-sensor

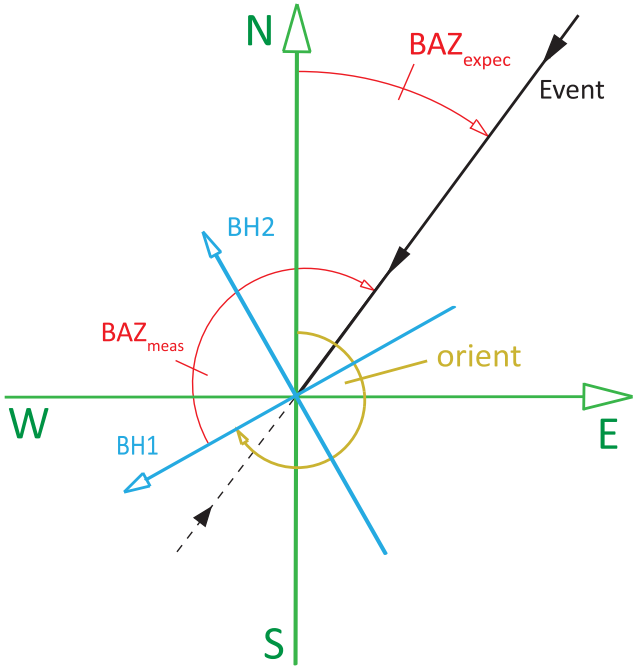

Figure 2. Principle of particle motion measurements to obtain horizontal sensor orientations. For isotropic and homogeneous propagation media, the particle motion is contained within the radial plane connecting the receiver and the source. In the horizontal plane, *P*-wave and Rayleigh wave polarizations thus provide apparent backazimuth estimates (BAZ_{meas}) between the station's 'north' component (here BH1, in blue) and the great circle event path (solid black line). Comparing BAZ_{meas} to the expected backazimuth angle BAZ_{expec}, yields the sensor orientation *orient* (yellow). The thin dashed line indicates the 180° ambiguity to be considered for *P*-wave polarization measurements (if BAZ_{expec} is unknown). For Rayleigh waves, retrograde elliptical motions are assumed, which eliminates any ambiguity.

anisotropy, acquired at crustal or upper mantle levels. *P*-wave particle motion does not integrate anisotropy along the entire ray path but is instead sensitive to anisotropy within the last *P* wavelength beneath the receiver (Schulte-Pelkum *et al*. 2001). The anisotropy-induced deviation depends on the dominant period used in the analysis, leading to a possible frequency-dependent deviation of particle motion from the direction of propagation and offering a method to potentially constrain the vertical distribution of anisotropy.

Schulte-Pelkum *et al*. (2001), Fontaine *et al*. (2009) and Wang *et al*. (2016, for synthetic waveforms) showed that sub-sensor anisotropy generates a 180° periodicity in the deviation of particle motion, whereas upper mantle heterogeneities and dipping interfaces generate a 360° periodicity. Observations of the periodicity in the P-pol deviation therefore provide a robust diagnostic of its origin. The amplitude of anisotropy-induced deviations in P-pol measurements is up to ±10° in an olivine single crystal, as calculated from the Christoffel equation and olivine single crystal elastic stiffness parameters (Mainprice 2015). Seismological observations of P-pol deviations deduced from teleseismic events recorded at the terrestrial permanent CEA (Commissariat à l'Energie Atomique) station PPTL on Tahiti (Fontaine *et al*. 2009) display variations with a 180° periodicity and an amplitude of up to ±7°, consistent with the trend of the regional upper mantle anisotropy pattern deduced from SKS splitting (Fontaine *et al*. 2007; Barruol *et al*. 2009). In the present study, we searched for a curve $\delta(\theta)$ fitting such deviations (Schulte-Pelkum *et al*. 2001; Fontaine *et al*. 2009) for stations providing eight or more measurements covering at least three quadrants of back-azimuths

$$\delta(\theta) = BAZ_{expec} - BAZ_{meas}(\theta) = A_1 + A_2\sin(\theta) + A_3\cos(\theta) + A_4\sin(2\theta) + A_5\cos(2\theta), \quad (2a)$$

where θ is the expected event back-azimuth in degrees; A_1 the station misorientation; A_2 and A_3 depend on the lateral heterogeneity – dipping of the interface but also dipping of the anisotropic axis – and A_4 and A_5 are the coefficients of anisotropy under the station, for the case of a horizontal symmetry axis (Fontaine *et al*. 2009). Adding 360°, taking the modulo 360° of eq. (2a) and combining with eq. (1) leads to an expression for the horizontal OBS orientation as a function of the expected backazimuth θ.

$$orient(\theta) = A_1 + A_2\sin(\theta) + A_3\cos(\theta) + A_4\sin(2\theta) + A_5\cos(2\theta). \quad (2b)$$

Since the OBSs do not rotate after settling on the seafloor, orientations are constant over time and parameter A_1 represents the misorientation value for the seismometer.

We estimate P-pol using FORTRAN codes (Fontaine *et al*. 2009) to analyse the *P*-wave particle motion in the selected time window, using principal component analyses (PCAs) of three different data covariance matrices (2 PCA in 2-D using horizontal components, and longitudinal and vertical components, respectively, and 1 PCA in 3-D using all three seismic components) to retrieve the following measures: (1) apparent back-azimuth angle (BAZ_{meas}) in the horizontal plane derived from the PCA of the three components; (2) apparent incidence angle (INC_{app}) derived from the PCA of the longitudinal and vertical components; (3) error of the apparent incidence angle $ER\_INC_{app} = \tan^{-1}\sqrt{\beta_2/\beta_1} \cdot 180°/\pi$; (4) signal-to-noise ratio $SNR = (\varepsilon_1 - \varepsilon_2)/\varepsilon_2$ (De Meersman *et al*. 2006); (5) degree of rectilinearity of the particle motion in the horizontal plane $CpH = 1 - \varepsilon_2/\varepsilon_1$ and (6) in the radial-vertical plane $CpZ = 1 - \beta_2/\beta_1$. *CpH* and *CpZ* are equal to 1 for purely linear polarizations and to 0 for circular polarizations. The eigenvalues β_i (2-D PCA of longitudinal and vertical components) and ε_i (2-D PCA of horizontal components) obey $\beta_1 \geq \beta_2$ and $\varepsilon_1 \geq \varepsilon_2$, respectively.

We selected teleseismic earthquakes of $M_w \geq 6.0$ and epicentral distances of up to 90° from the centre of the RHUM-RUM network (La Réunion Island, 21.0°S and 55.5°E). To increase the number of measurements at each station, we also considered regional earthquakes with epicentral distances of up to 20° with $M_w \geq 5.0$. Earthquake locations were taken from the National Earthquake Information Center (NEIC).

For each P-pol measurement, we removed means and trends from displacement data and applied a Hanning taper. Data windows were then taken from 15 s before to 25 s after the predicted *P*-wave arrival times (iasp91 model, Kennett & Engdahl 1991). No data downsampling was required. To check for any frequency-dependent results, obtain the highest possible *SNR* and retrieve the maximum amount of information from the data set, each measurement was performed in nine different passbands (using a zero-phase, 2-pole Butterworth filter): 0.03–0.07, 0.03–0.09, 0.03–0.12, 0.03–0.20, 0.05–0.09, 0.05–0.12, 0.07–0.10, 0.07–0.12 and 0.13–0.20 Hz all close to the long-period noise notch, a local minimum of noise amplitudes in the oceans that is observed worldwide (Webb 1998).

P-pol measurements were retained if they met the following criteria: $SNR \geq 15$, $CpH \geq 0.9$, $CpZ \geq 0.9$, $ER\_INC_{app} \leq 15°$ and $ER\_BAZ_{meas} \leq 15°$. ER_BAZ_{meas} is the error of an individual back-azimuth estimate (see error Section 4.3.1, eq. 3). For

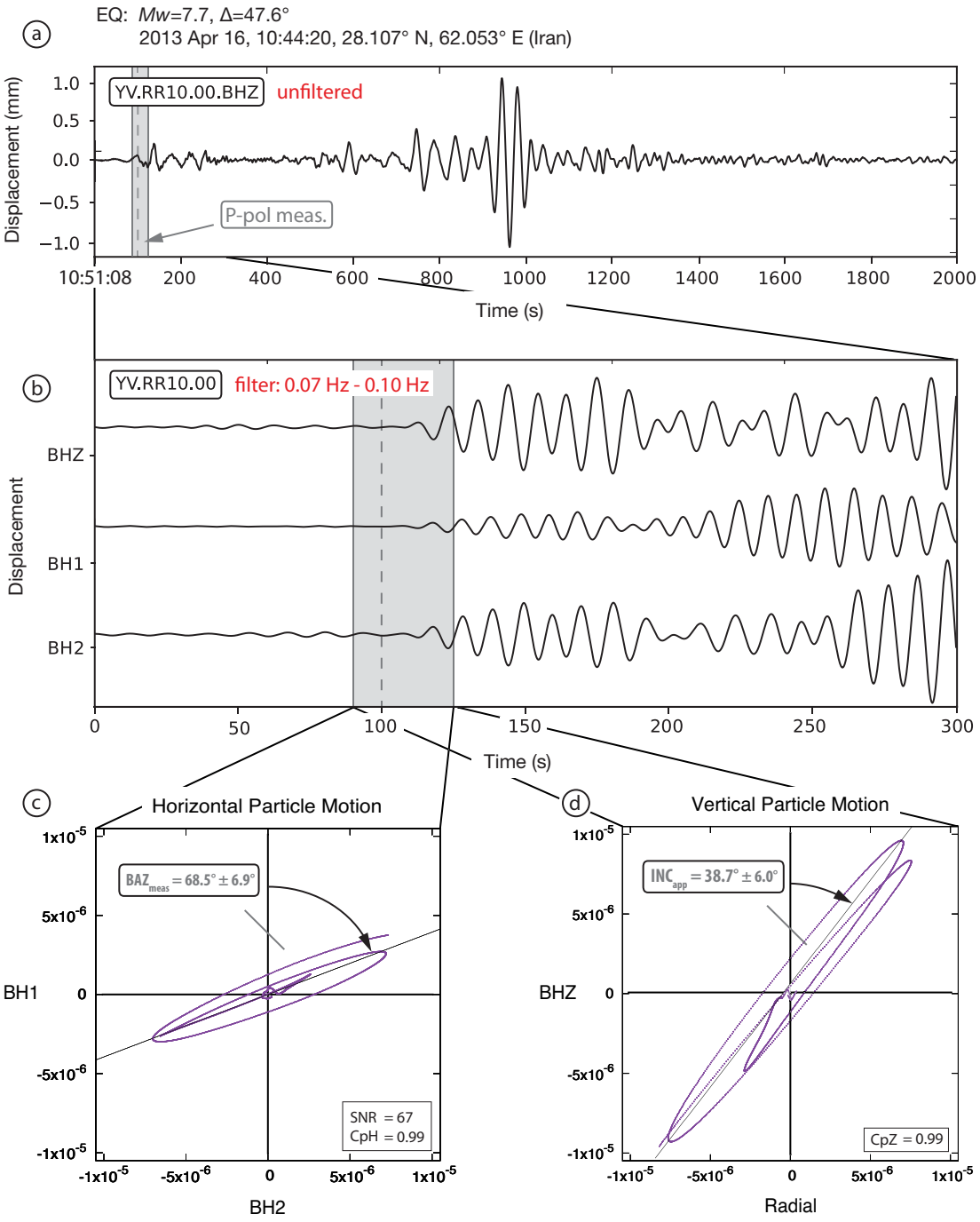

Figure 3. Example of an individual P-pol measurement at DEPAS station RR10 for the $M_w = 7.7$ Iran earthquake of 2013 April 16: (a) raw trace of vertical wideband seismogram, showing the 40 s P-pol measurement window (grey shaded box); (b) three-component seismograms filtered between 0.07–0.10 Hz (best filter for this station) with the P-pol measurement time window (shaded grey) and the predicted *P*-wave onset (dashed line); (c) horizontal particle motion during the P-pol window, used to estimate event back-azimuth BAZ_{meas}; (d) radial-vertical particle motion, used to estimate the apparent incidence angle INC_{app}.

final station orientations, we used the passband with the highest summed *SNR*. This procedure ensured that, for a given station, all measurements were obtained in the same frequency band and hence were affected by the same crustal and upper mantle layer. The individual P-pol measurements were visually checked, based on waveform appearance and the resulting strength of polarization.

Fig. 3 shows an example of an individual P-pol measurement of good quality for DEPAS station RR10, using the Iran $M_w = 7.7$ earthquake of 2013 April 16. The passband filter 0.07–0.10 Hz delivered the highest *SNR* sum for all retained events for this station, leading to a measured back-azimuth of $BAZ_{meas} = 68.5° \pm 6.9°$ (Fig. 3c) for the given event. Using eq. (1), we calculate the station orientation for this measurement to be $orient = 287.1° \pm 6.9°$. Error quantifications of individual back-azimuth estimates and of averaged station orientations are presented in Section 4.3. The apparent incidence angle for this seismogram is $INC_{app} = 38.7° \pm 6.0°$ (Fig. 3d).

4.2 Polarization of regional and teleseismic Rayleigh waves (R-pol)

Rayleigh waves are expected to propagate within the vertical plane along the great circle path, linking source and receiver. In the absence of anisotropy and large-scale heterogeneities along the ray-path, the horizontal polarization of Rayleigh waves (and *P*-waves) is parallel to the theoretical, expected back-azimuth. As fundamental Rayleigh waves propagate with a retrograde particle motion, there is no 180° ambiguity in the measured back-azimuths.

Crustal and upper mantle heterogeneities and anisotropy, however, influence the ray path geometry and therefore the Rayleigh wave polarizations recorded at a station. We do not attempt to estimate azimuthal deviations of R-pol off the great-circle plane because we have only 13 months of data available from the temporary OBS deployment, and because Rayleigh waves, as opposed to *P*-waves, are affected by seismic anisotropy and ray-bending effects over their entire path. Instead, we simply average our measurements over all individual *orient* estimates for a given station to determine the sensor's orientation, as suggested by Laske (1995).

Although Stachnik *et al*. (2012) previously used Rayleigh-wave polarizations to determine back-azimuths, our analysis method is quite different. We decompose three-component seismograms using an S-transform to detect polarized signals in the time *and* frequency domains. This was done using the software 'polfre' (Schimmel & Gallart 2004; Schimmel *et al*. 2011). The measurement is multiplied by a Gaussian-shaped window whose length is frequency-dependent in order to consider an equal number of wave *cycles* in each frequency band. The semi-major and semi-minor vectors of the instantaneous ground motion ellipses are then calculated in the different time-frequency sub-domains, and summed over a second moving window of sample length *wlen* to obtain the degree of elliptical polarization in the vertical plane (*DOP*) and corresponding back-azimuths. This approach rejects Love waves. The *DOP* is a measure of the stability of polarization over time and varies between 0 and 1, with 1 indicating a perfectly stable elliptical particle motion in the vertical plane. We use the following thresholds for retaining R-pol measurements: $DOP_{\min} = 0.9$; $cycles = 2$; $wlen = 4$; $linearity \leq 0.3$ (1 = purely linear polarization, 0 = circular polarization); $DOP_{\text{power}} = 4$ (controls the number of polarized signals above threshold $DOP_{\min}$); $nflen = 2$ (number of neighbouring frequencies to average); and $nfr = 512$ (number of different frequency bands within the chosen corner frequencies).

We selected regional and teleseismic earthquakes of $M_w \geq 6.0$ and epicentral distances of up to 160° from La Réunion Island. Earthquake locations were taken from the NEIC.

R-pol measurements were performed on three-component displacement seismograms, extracted in 300 s windows starting from predicted Rayleigh phase arrivals, assuming a 4.0 km s^{-1} fundamental phase velocity as a compromise between continental and oceanic lithosphere (PREM model, Dziewonski & Anderson 1981). Seismograms were low-pass filtered to decimate the data by a factor of 32 and subsequently bandpass filtered between 0.02–0.05 Hz (20–50 s), corresponding to the long-period noise notch between the primary and secondary microseisms (period 2–20 s) and the long period seafloor compliance noise (period >50 s).

R-pol measurements were retained if at least 7000 single measurement points from the sub-windows of the 300 s window were obtained, all meeting the criteria stated above. Under these conditions, the best estimate of event back-azimuth is determined as the arithmetic mean of all back-azimuth values in the time window.

Fig. 4 shows a R-pol measurement of good quality, for the same station and earthquake as in Fig. 3 (P-pol measurement). The incoming Rayleigh wave is clearly visible on the raw vertical seismogram (Fig. 4a) and on the filtered three components (Fig. 4b). The maximum *DOP* (Fig. 4c) with corresponding back-azimuth values (Fig. 4d) provide the best estimate of event back-azimuth for this example with $BAZ_{\text{meas}} = 57.9° \pm 12.6°$. Using eq. (1), the station orientation is $orient = 297.6° \pm 12.6°$ for this individual measurement. Error quantifications of individual and averaged station orientations are presented in Section 4.3.

4.3 Error calculation

Errors on individual measurements and on average station orientations should be quantified in order to provide the end-user an idea of the orientation accuracy and to compare between orientation methods. We explain our approach to calculating uncertainties of individual P-pol and R-pol measurements in Section 4.3.1, of uncertainties of averaged station orientations in Section 4.3.2, and of uncertainties after fitting P-pol orientations via eq. (2b) in Section 4.3.3.

4.3.1 Errors in individual back-azimuth measurements

To calculate errors of individual P-pol measurements, we follow the approach of Reymond (2010) and Fontaine *et al*. (2009):

$$ER\_BAZ_{\text{meas, Ppol}} = \tan^{-1}\sqrt{\frac{\varepsilon_2}{\varepsilon_1}} \cdot \frac{180°}{\pi}, \tag{3}$$

with ε_i the eigenvalues of the data covariance matrix in the horizontal plane (Section 4.1).

Errors of individual R-pol measurements are given as standard deviation around the arithmetic mean of the station's single back-azimuth estimates in the selected Rayleigh wave time window:

$$ER\_BAZ_{\text{meas, Rpol}} = \sqrt{\frac{1}{M}\sum_{i=1}^{M}(x_i - \bar{x})^2}, \tag{4}$$

with M the number of measurement points and x the single back-azimuth measurements.

4.3.2 Errors on averaged station orientations

Our best estimate for a station's orientation and its uncertainty is obtained by averaging over all N individual measurements at this station. To conform with the present literature, we calculated both circular mean and median averages. For our data, N ranges between 2 and 20 for P-pol, and between 3 and 60 for R-pol (Table 1).

We define the error of the circular mean as twice the angular deviation. The angular deviation is analogous to the linear standard deviation (Berens 2009), hence twice its value corresponds to a 95 per cent confidence interval. The equation is

$$ER\_Orient_{\text{circ\_mean}} = 2\sqrt{2(1-R)} \cdot \frac{180°}{\pi}, \tag{5}$$

where R is the mean resultant length of the circular distribution, defined as

$$R = \frac{1}{N} \cdot \sqrt{\left(\sum_{i=1}^{N} \cos orient_i\right)^2 + \left(\sum_{i=1}^{N} \sin orient_i\right)^2}, \tag{6}$$

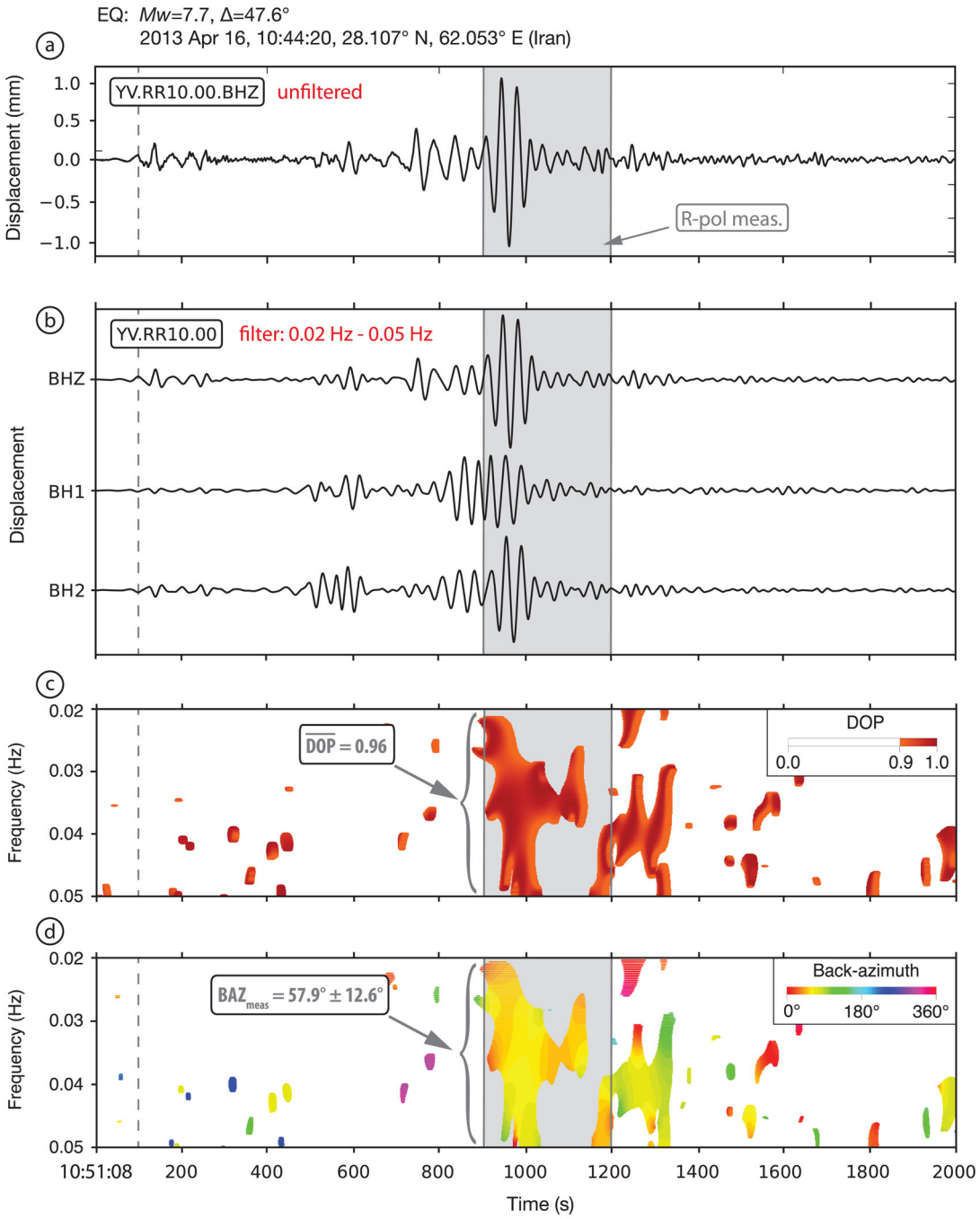

Figure 4. Example of an individual R-pol measurement at DEPAS station RR10 for the $M_w = 7.7$ Iran earthquake of 2013 April 16 (same event as in Fig. 3): (a) raw trace of vertical wideband seismogram, showing the predicted *P*-wave onset (dashed line) and the 300 s R-pol measurement window (grey shaded box); (b) three-component seismograms filtered between 0.02–0.05 Hz with R-pol measurement window; (c) distribution of $DOP \geq 0.9$ in the time-frequency plane; (d) corresponding signal back-azimuths in the time-frequency plane.

with N orientation angles *orient*. For the median, we use the scaled median absolute deviation (*SMAD*) as its measure of error, similar to Stachnik *et al*. (2012). The *MAD* is calculated as:

$$MAD = median_i \left(\left| orient_i - median_j \left(orient_j \right) \right| \right), \quad (7)$$

with i and j iterating over the N orientation angles *orient*. The *MAD* value is multiplied by a factor S, which depends on the data distribution. Since this is difficult to determine for our small sample sizes N, we assume a Gaussian distribution, which implies $S = 1.4826$ and makes the *SMAD* equivalent to the standard deviation (Rousseeuw & Croux 1993). The equation for the error is therefore:

$$ER\_Orient_{\text{median}} = 2 \cdot 2.4826 \cdot MAD = 2 \cdot SMAD \quad (8)$$

which also corresponds to a 95 per cent confidence interval.

In order to prevent outliers in the R-pol measurements from skewing the results, we calculated 95 per cent confidence intervals for both the circular mean and median, retained only observations within these intervals, and recalculated the circular mean and median averages and their errors

Table 1. Horizontal sensor orientations of the 57 RHUM-RUM OBSs derived from *N* averaged *P*-wave and Rayleigh wave polarization measurements. Orientation angles are clockwise from geographic North to the BH1 component (BH1 is 90° anti-clockwise from BH2, see Fig. 2). 13 stations did not record useable data (red boxes), 4 stations showed very high noise levels (orange boxes)—see Stähler *et al*. (2016) for details. Grey boxed mark INSU-IPGP stations, all other stations were provided by DEPAS or GEOMAR. P-pol yielded orientation estimates and uncertainties for 31 stations, and estimates corrected for anisotropy and dipping discontinuities at seven stations ('Deviation Fit'). R-pol yielded orientation estimates and uncertainties for 40 stations. 'C1' indicates culled data similar to the approach of Stachnik *et al*. (2012), as described in Section 4.3.2.

STATION	P-pol						R-pol ('C1')			
	N	DEVIATION FIT (ERR)		CIRC MEAN (2*STD)		MEDIAN (2**SMAD*)	*N*	CIRC MEAN (2*STD)		MEDIAN (2**SMAD*)
RR01	5	—		342°	(22°)	348° (17°)	7	323°	(14°)	5	328° (2°)
RR02	—	—		—		—	—	—		—	—
RR03	0	—		—		—	18	76°	(18°)	19	79° (23°)
RR04	—	—		—		—	—	—		—	—
RR05	0	—		—		—	3	45°	(8°)	3	45° (13°)
RR06	5	—		124°	(12°)	123° (18°)	14	124°	(11°)	10	122° (4°)
RR07	2	—		46°	(5°)	46° (7°)	6	48°	(10°)	6	48° (12°)
RR08	4	—		154°	(10°)	154° (14°)	14	161°	(18°)	13	156° (13°)
RR09	3	—		135°	(22°)	133° (33°)	14	125°	(16°)	14	124° (21°)
RR10	8	—		288°	(11°)	286° (11°)	21	286°	(18°)	21	287° (19°)
RR11	4	—		40°	(17°)	39° (15°)	15	43°	(15°)	15	44° (17°)
RR12	5	—		26°	(5°)	26° (3°)	10	27°	(9°)	10	26° (9°)
RR13	3	—		314°	(8°)	315° (14°)	12	315°	(14°)	12	314° (20°)
RR14	4	—		19°	(8°)	18° (4°)	16	15°	(16°)	16	15° (21°)
RR15	—	—		—		—	—	—		—	—
RR16	2	—		163°	(10°)	163° (15°)	10	162°	(12°)	8	166° (9°)
RR17	0	—		—		—	11	247°	(9°)	11	247° (9°)
RR18	3	—		295°	(6°)	295° (6°)	8	292°	(21°)	8	292° (26°)
RR19	3	—		120°	(5°)	121° (2°)	8	120°	(18°)	6	118° (7°)
RR20	0	—		—		—	14	159°	(22°)	14	160° (29°)
RR21	0	—		—		—	12	281°	(10°)	11	282° (10°)
RR22	3	—		287°	(9°)	285° (8°)	14	285°	(15°)	10	285° (7°)
RR23	—	—		—		—	—	—		—	—
RR24	—	—		—		—	—	—		—	—
RR25	4	—		281°	(6°)	282° (5°)	20	276°	(17°)	20	276° (25°)
RR26	4	—		138°	(6°)	137° (6°)	12	146°	(18°)	12	145° (21°)
RR27	0	—		—		—	0	—		0	—
RR28	18	72°	(4°)	72°	(12°)	72° (12°)	51	70°	(20°)	51	71° (22°)
RR29	15	266°	(4°)	267°	(7°)	267° (8°)	48	266°	(13°)	48	267° (15°)
RR30	4	—		293°	(9°)	293° (10°)	12	292°	(13°)	12	290° (15°)
RR31	4	—		75°	(6°)	75° (6°)	22	76°	(17°)	23	78° (24°)
RR32	—	—		—		—	—	—		—	—
RR33	0	—		—		—	0	—		0	—
RR34	8	131°	(8°)	131°	(4°)	130° (6°)	39	134°	(21°)	36	135° (16°)
RR35	—	—		—		—	—	—		—	—
RR36	18	225°	(3°)	227°	(19°)	225° (12°)	60	226°	(19°)	56	226° (16°)
RR37	0	—		—		—	0	—		0	—
RR38	20	314°	(2°)	313°	(7°)	314° (7°)	32	314°	(33°)	28	320° (23°)
RR39	—	—		—		—	—	—		—	—
RR40	10	229°	(7°)	229°	(21°)	231° (25°)	44	228°	(15°)	42	229° (14°)
RR41	2	—		93°	(10°)	93° (15°)	8	96°	(24°)	6	90° (13°)
RR42	—	—		—		—	—	—		—	—
RR43	0	—		—		—	18	104°	(18°)	19	104° (24°)
RR44	0	—		—		—	7	169°	(28°)	6	166° (21°)
RR45	0	—		—		—	0	—		0	—
RR46	3	—		150°	(7°)	150° (12°)	19	139°	(21°)	19	139° (21°)
RR47	0	—		—		—	10	124°	(15°)	9	129° (10°)
RR48	0	—		—		—	10	55°	(11°)	10	55° (11°)
RR49	—	—		—		—	—	—		—	—
RR50	11	350°	(13°)	348°	(9°)	348° (12°)	22	348°	(16°)	20	350° (14°)
RR51	—	—		—		—	—	—		—	—
RR52	6	—		29°	(10°)	29° (7°)	27	29°	(17°)	27	28° (23°)
RR53	8	—		99°	(11°)	101° (8°)	28	99°	(18°)	25	97° (13°)
RR54	—	—		—		—	—	—		—	—
RR55	4	—		251°	(15°)	250° (14°)	16	253°	(19°)	17	256° (25°)
RR56	4	—		340°	(13°)	338° (14°)	13	338°	(13°)	13	338° (21°)
RR57	—	—		—		—	—	—		—	—

on the retained data. This procedure is equivalent to the 'C1' data culling of Stachnik *et al*. (2012).

4.3.3 Errors in anisotropy-fitted P-pol orientations

For seven stations providing a large enough number of data ($N \geq 8$) with a wide enough back-azimuthal coverage (at least three quadrants), the observed P-pol measurements were fit to a curve taking into account the presence of seismic anisotropy and dipping discontinuities beneath the station (eq. 2b). We used gnuplot 5.0 (Williams & Kelley 2015) to perform the fittings. As explained by Young (2015, p. 62), the asymptotic standard error fits estimated by gnuplot must be divided by the square root of chi-squared per degree of freedom (called FIT_STDFIT in gnuplot) to obtain the true error. The resulting fitting curves drastically reduce the error of polarization measurements and therefore provide more accurate sensor orientations. For example, for station RR28 where $N = 18$, the error obtained from the curve fitting (4°) is three times smaller than the errors of the circular mean (12°) or median (12°) (Fig. 5).

5 RESULTS

Exemplary for INSU-IPGP station RR28, the individual back-azimuth measurements and their errors are illustrated as a function of the expected back-azimuths in Figs 5 (P-pol) and 6 (R-pol). Averaged orientation estimates for each OBS and their errors were obtained for 40 out of 57 OBSs and are summarized in Table 1. For 13 OBSs we could not determine orientations due to instrument failures (Table 1, in red); on four other OBSs, data were too noisy to obtain reliable measurements of either P-pol or R-pol (Table 1, in orange). Orientation results of the P-pol and R-pol methods are in good agreement, with a maximum difference of 20° (RR01, Fig. 7a). Comparing the two methods to each other, the orientations differ in average by 3.1° and 3.7° for circular mean and median statistics, respectively. OBS orientations are evenly distributed over the range of possible azimuths (Fig. 7b, for R-pol), as might be expected for free-fall instruments dropped from a ship.

5.1 P-pol orientations

197 individual P-pol measurements, based on 48 earthquakes, yielded sensor orientation estimates for 31 stations. Signal-to-noise ratios (*SNRs*) of individual events ranged from 15 to 1603, averaging around 100. More than 75 per cent of the P-pol measurements were optimal in the frequency band of 0.07–0.10 Hz (10–14 s of period). Individual P-pol errors (eq. 3) are typically smaller than 10°. Uncertainties for the circular mean and median (eqs 5 and 8, 95 per cent confidence intervals) average 11° for all stations and both statistics, with a maximum error of 33° at RR09 (Table 1).

We obtained P-pol fits for underlying seismic anisotropy and dipping discontinuities at seven stations using eq. (2b) (Table 1, 'Deviation Fit' column), with a minimum error of 2° at RR38, a maximum error of 13° at RR50, and an average uncertainty of only 6°. These anisotropy-fit OBS orientations are the most accurate ones established in this study.

5.2 R-pol orientations

749 individual R-pol measurements, based on 110 earthquakes, yielded sensor orientations for 40 stations. *DOP*, the degree of elliptical polarization in the vertical plane, averages 0.97 over all measurements. Errors of individual R-pol measurements (eq. 4) range typically between 10° and 25°, but can be as high as 50°, probably due to seismic anisotropy, ray-bending effects and interference with ambient noise Rayleigh waves. We integrated all measurements into our analysis, regardless of their individual errors. Rejecting measurements with errors of individual back-azimuth estimates larger than 25° did not change the averaged orientations, but decreased their circular mean and median errors (eqs 5 and 8, 95 per cent confidence intervals) by up to 10°. Nevertheless, we chose to use as many measurements as available to calculate the average

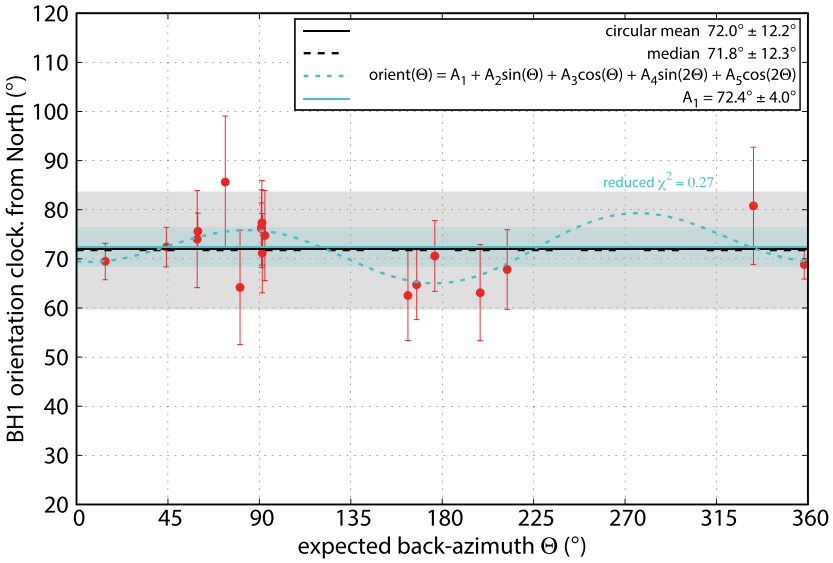

Figure 5. Summary of $N = 18$ *P*-wave polarization (P-pol) measurements obtained for INSU-IPGP station RR28 in the (optimal) frequency passband of 0.07–0.10 Hz. Red dots = individual orientation estimates (eq. 1) over the expected back-azimuths; red bars = errors of individual P-pol estimates (eq. 3); solid black line = circular mean of the N measurements; dashed black line = circular median of the N measurements; dashed cyan line = sinusoidal correction for anisotropy and dipping discontinuities beneath the station (eq. 2b); solid cyan line = constant A_1 (eq. 2b), which is our best estimate of sensor orientation; grey box shows = 95 per cent confidence interval of median orientation (eq. 8), cyan box = error interval of sensor orientation A_1.

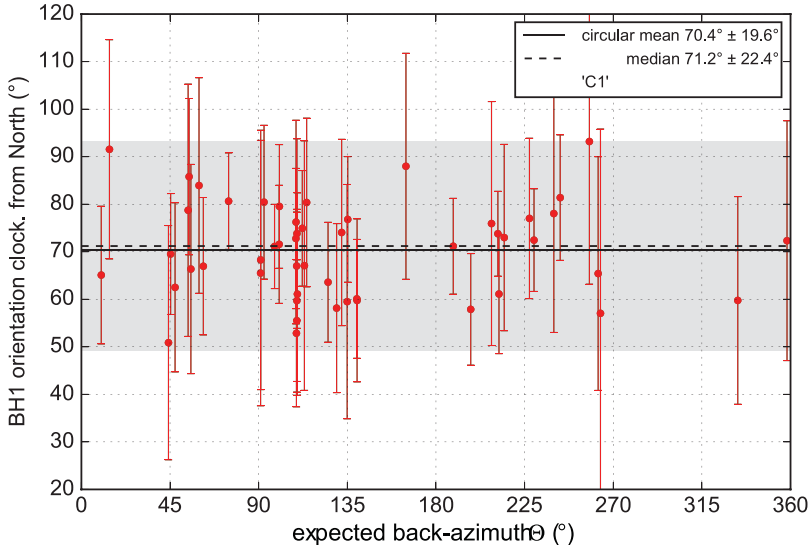

Figure 6. Summary of $N = 51$ Rayleigh wave polarization (R-pol) measurements for INSU-IPGP station RR28 in the frequency passband of 0.02–0.05 Hz. Red dots = individual orientations estimates (eq. 1) over the expected back-azimuths; red bars = errors of individual R-pol estimates (eq. 4); solid black line = circular mean of the N measurements; dashed black line = median; grey box = 95 per cent confidence interval of median orientation (eq. 8). 'C1' indicates that shown data are culled, as specified in Section 4.3.2.

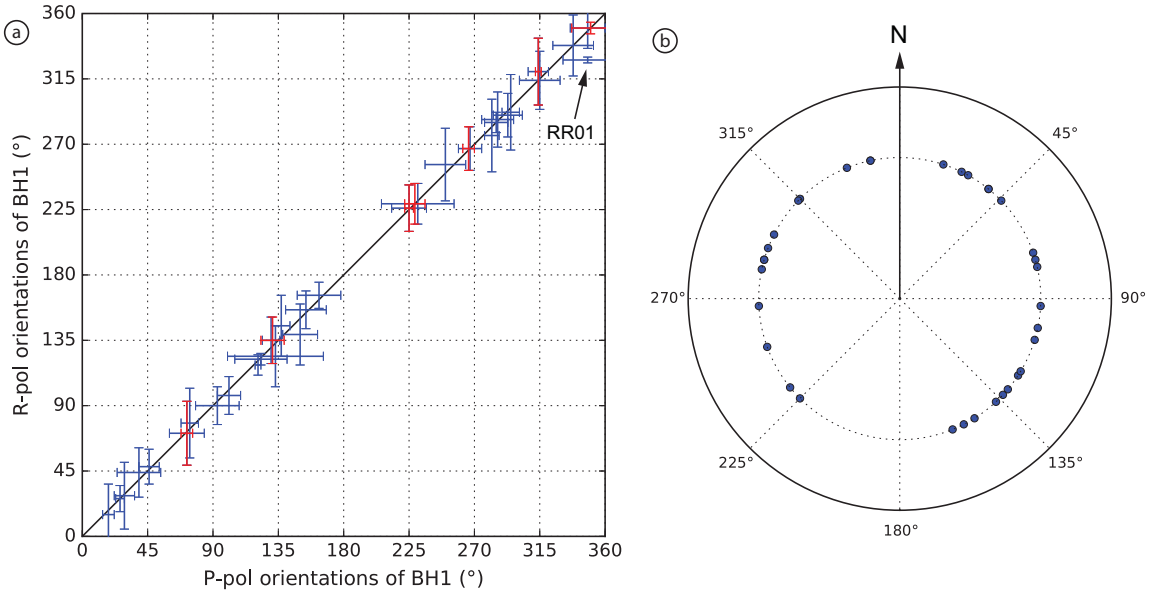

Figure 7. Overall OBS orientation results (median values). (a) Orientations obtained from P-pol versus R-pol. Centres of blue crosses = estimates for 31 OBS where medians could be obtained for both P-pol and R-pol; blue crosses = errors (95 per cent confidence intervals, eq. 8); black line indicates identical P-pol and R-pol orientations. 'RR01' indicates station RR01, the only station whose value + error does not fall on this line. Centres of red crosses = A_1 values of P-pol curve fits (eq. 2b) versus R-pol medians; red crosses = their 95 per cent confidence intervals and gnuplot fit errors, respectively. (b) Blue dots = horizontal orientations of all 40 BH1 components with respect to geographic North, obtained from R-pol.

R-pol OBS orientations. Errors for the circular mean and median average 16° for both statistics, with a maximum error of 33° at RR38 (Table 1).

6 DISCUSSION

Our results show good agreement between the P-pol and R-pol methods (Fig. 7a). The P-pol method usually delivers more accurate sensor orientations, particularly for the seven stations where we could fit for the orientation deviations caused by seismic anisotropy and dipping discontinuities beneath the stations (Schulte-Pelkum *et al*. 2001; eq. 2b). The best period range for this P-pol analysis was 10–14 s, which corresponds to P wavelengths ranging 80 to 110 km, suggesting a dominant mantle signature in the polarization deviations. This suggestion is supported by the fact that the crust is (almost) absent along Mid-Ocean Ridges, with oceanic crustal thicknesses in the Indian Ocean ranging 6–10 km excluding possible underplated layer, or up to 28 km including a possible underplated layer (Fontaine *et al*. 2015). The good agreement between the anisotropy-fit P-pol and R-pol (with Rayleigh waves of period 20–50 s being most sensitive to shear-velocity variations with depth) further supports the suggestion that the obtained orientations are

not significantly biased by seismic anisotropy and heterogeneities originating at crustal levels.

Uncertainties are larger for P-pol and R-pol than for the anisotropy-corrected P-pol estimates, but the orientations provided by these three algorithms are fully consistent. The obtained circular mean and median orientations do not appear to be significantly biased by underlying seismic anisotropy and dipping discontinuities. We find that 8 is a reasonable minimum number of good quality P-pol measurements required (if obtained in at least three back-azimuth quadrants) to obtain sensor orientations with stable uncertainties, which is close to the value of 10 proposed by Wang *et al*. (2016).

In contrast to *P*-wave polarizations, where deviations can be quantified and explained by seismic anisotropy and dipping discontinuities within the last wavelength beneath the sensor (Schulte-Pelkum *et al*. 2001), the quantitative effects of those factors on Rayleigh waves are much more complex. For example, for teleseismic Rayleigh waves of periods of 20–50 s (as used for our R-pol analysis), Pettersen & Maupin (2002) observed polarization anomalies of several degrees in the vicinity of the Kerguelen hotspot in the Indian Ocean. These anomalies decreased at increasing period and cannot be explained by geometrical structures; instead, the authors suggested seismic anisotropy located in the lithosphere north of the Kerguelen plateau. However, in light of the good agreement between our P-pol and R-pol measurements that featured good azimuthal coverage (Figs 5 and 6), we conclude that simply averaging the R-pol measurements for sensor orientations gives valid results, even without inverting them for local and regional anisotropy patterns. By simply averaging the orientations in the potentially complex case of Rayleigh wave polarizations, it is not surprising that the stations' averaged orientation error is slightly higher for R-pol (16°) than for P-pol (11°). For R-pol, one might be able to decrease the orientation errors by analysing the large-scale anisotropic pattern using for example SKS splitting measurements, by applying stricter criteria on individual R-pol measurements (e.g. *cycles* > 2), and/or by analysing the signals in more selective period ranges (compared to 20–50 s).

The number of individual measurements that we performed in this study is usually smaller for P-pol than for R-pol due to lower signal amplitudes of *P*-waves compared to Rayleigh waves, especially for ocean-bottom instruments recording in relatively high ambient noise. For 9 out of 44 stations we were able to quantify station misorientations only via R-pol, confirming the advantage of attempting both of these two independent orientation methods.

Based on a composite French-German ocean-bottom seismometer (OBS) network, the RHUM-RUM experiment enabled the comparison of DEPAS/GEOMAR and INSU-IPGP stations. We obtained up to four times more P-pol and two times more R-pol measurements on the broad-band INSU-IPGP stations than on the wideband DEPAS/GEOMAR seismometers. Despite this difference, the final uncertainties are rather similar for both sensor types. The significantly lower numbers of P-pol and R-pol measurements on the DEPAS and GEOMAR OBS are due to their significantly higher self-noise levels at periods >10 s, especially on horizontal components (Stähler *et al*. 2016), as compared to the INSU-IPGP instruments.

Attempting to *orient* OBS may also help diagnose instrumental troubles. For example, for several stations, P-pol and R-pol orientations were found to vary within unexpectedly large ranges and with anomalous patterns, despite waveform data of apparently good quality and despite good success for our routine at all other stations. This enabled the diagnosis of swapped horizontal components at the problematic stations as the cause for the aberrant observations. A detailed explanation of this and other problems is provided in the Supporting Information.

Computation algorithms for P-pol and R-pol are automated, each requiring about 90 minutes of execution time per station on a desktop computer. For P-pol, however, a visual check of the resulting strength of polarization is required.

7 CONCLUSIONS

This work presents two independent, automated methods for determining the absolute horizontal sensor misorientations of seismometers, based on estimates of back-azimuths of teleseismic and regional earthquakes, determined from 3-D particle motions of (1) *P*-waves and (2) Rayleigh waves.

The *P*-wave measurements followed the approach of Schulte-Pelkum *et al*. (2001) and Fontaine *et al*. (2009) and are based on principal component analyses of the three seismic components in nine different frequency passbands, allowing one to test the measurement stability as a function of the signal's dominant frequency content. We show that if 8 or more individual measurements at a given station are available within at least 3 back-azimuthal quadrants, the stations' orientation can be corrected for the underlying seismic anisotropy and dipping discontinuities beneath the station. For Rayleigh waves, we determined the stability of the elliptical particle motion in the vertical plane using a time-frequency approach (Schimmel & Gallart 2004; Schimmel *et al*. 2011).

We applied both methods to the 44 functioning ocean-bottom seismometers (OBS) of the RHUM-RUM project around La Réunion Island in the Indian Ocean. We successfully oriented 31 OBS from P-polarizations and 40 OBS from Rayleigh polarizations. Averaged P-pol and R-pol orientation estimates are fully consistent within their respective error bars. The P-pol method may be as accurate as 6° on average when taking into account sub-sensor seismic anisotropy and dipping discontinuities, demonstrating a strong potential for this approach to simultaneously determine sensor orientation and underlying upper mantle anisotropy.

Although R-pol is intrinsically less accurate than P-pol in orienting OBS, the larger number of Rayleigh waves available during a temporary experiment allows the determination of orientation at sites where P-pol may fail.

We demonstrate that the two orientation methods work reliably, independently, and provide consistent results, even though the application to the RHUM-RUM data set was challenging due to (i) the short duration of data (as little as 6 months for some sites that did not record throughout the deployment); (ii) the high self-noise levels on the horizontal components of most of the instruments (DEPAS/GEOMAR type); and (iii) the variety of geodynamic and geological conditions at the deployment sites, such as rocky basement on ultraslow versus fast spreading Mid-Ocean Ridges, thick sedimentary covers around La Réunion Island (up to 1000 m, Whittaker *et al*. 2013), and potential plume-lithosphere and plume-ridge interactions; all likely to cause complex patterns of seismic anisotropy and distorted wavepaths. Successfully demonstrated under challenging deep-sea conditions, these two methods could equally help to determining accurate misorientations of land stations.

ACKNOWLEDGEMENTS

The RHUM-RUM project (www.rhum-rum.net) was funded by ANR (Agence Nationale de la Recherche) in France (project

ANR-11-BS56-0013), and by DFG (Deutsche Forschungsgemeinschaft) in Germany (grants SI1538/2-1 and SI1538/4-1). Additional support was provided by CNRS (Centre National de la Recherche Scientifique, France), TAAF (Terres Australes et Antarctiques Françaises, France), IPEV (Institut Polaire Français Paul Emile Victor, France), AWI (Alfred Wegener Institut, Germany), and by a EU Marie Curie CIG grant « RHUM-RUM » to K.S. We thank DEPAS (Deutsche Geräte-Pool für Amphibische Seismologie, Germany), GEOMAR (GEOMAR Helmholtz-Zentrum für Ozeanforschung Kiel, Germany) and INSU-IPGP (Institut National des Sciences de l'Univers - Institut de Physique du Globe de Paris, France) for providing the broad-band ocean-bottom seismometers (44 DEPAS, 4 GEOMAR, 9 INSU-IPGP). The RHUM-RUM data set (http://dx.doi.org/10.15778/RESIF.YV2011) has been assigned the FDSN network code YV and is hosted and served by the French RESIF data centre (http://seismology.resif.fr). Data will be freely available by the end of 2017. We thank cruise participants and crew members on *R/V Marion Dufresne*, cruise MD192 and on *R/V Meteor*, cruise M101. We acknowledge support from/discussions within TIDES COST Action ES1401. We used the open-source toolboxes GMT v.5.1.1 (Wessel *et al*. 2013), Gnuplot v.5.0 (Williams & Kelley 2015), Python v.2.7 (Rossum 1995), ObsPy v.0.10.2 (Beyreuther *et al*. 2010), and ObspyDMT v.0.9.9b (Scheingraber *et al*. 2013; Hosseini 2015). We are grateful to Martin Schimmel for providing his 'polfre' toolbox (v.04/2015) (Schimmel & Gallart 2004; Schimmel *et al*. 2011), and for his patience in answering our questions. This manuscript was greatly improved thanks to the suggestions of two anonymous reviewers. This is IPGP contribution 3806.

REFERENCES

Amante, C. & Eakins, B.W., 2009. NOAA Technical Memorandum NESDIS NGDC-24. National Geophysical Data Center, NOAA, doi:10.7289/V5C8276M.

Anderson, P.N., Duennebier, F.K. & Cessaro, R.K., 1987. Ocean borehole horizontal seismic sensor orientation determined from explosive charges, *J. geophys. Res.,* **92**(B5), 3573–3579.

Baker, G.E. & Stevens, J.L., 2004. Backazimuth estimation reliability using surface wave polarization, *Geophys. Res. Lett.,* **31**(9), doi:10.1029/2004GL019510.

Barruol, G., 2014. RHUM-RUM Marion Dufresne MD192 cruise report Sept–Oct 2012, 33, doi:10.13140/2.1.2492.0640.

Barruol, G., Suetsugu, D., Shiobara, H., Sugioka, H., Tanaka, S., Bokelmann, G.H.R., Fontaine, F.R. & Reymond, D., 2009. Mapping upper mantle flow beneath French Polynesia from broadband ocean bottom seismic observations, *Geophys. Res. Lett.,* **36**(14), doi:10.1029/2009GL038139.

Barruol, G., Deplus, C. & Singh, S., 2012. MD 192 / RHUM-RUM cruise, Marion Dufresne R/V, doi:10.17600/12200070.

Berens, P., 2009. CircStat: a MATLAB toolbox for circular statistics, *J. Stat. Softw.,* **31**(10), 1–21.

Beyreuther, M., Barsch, R., Krischer, L., Megies, T., Behr, Y. & Wassermann, J., 2010. ObsPy: a python toolbox for seismology, *Seismol. Res. Lett.,* **81**(3), 530–533.

De Meersman, K., van der Baan, M. & Kendall, J.-M., 2006. Signal extraction and automated polarization analysis of multicomponent array data, *Bull. seism. Soc. Am.,* **96**(6), 2415–2430.

Dziewonski, A.M. & Anderson, D.L., 1981. Preliminary reference Earth model, *Phys. Earth planet. Inter.,* **25**(4), 297–356.

Ekstrom, G. & Busby, R.W., 2008. Measurements of seismometer orientation at USArray transportable array and backbone stations, *Seismol. Res. Lett.,* **79**(4), 554–561.

Fontaine, F.R., Barruol, G., Tommasi, A. & Bokelmann, G.H.R., 2007. Upper-mantle flow beneath French Polynesia from shear wave splitting, *Geophys. J. Int.,* **170**(3), 1262–1288.

Fontaine, F.R., Barruol, G., Kennett, B.L.N., Bokelmann, G.H.R. & Reymond, D., 2009. Upper mantle anisotropy beneath Australia and Tahiti from *P* wave polarization: implications for real-time earthquake location, *J. geophys. Res.,* **114**(B3), doi:10.1029/2008JB005709.

Fontaine, F.R., Barruol, G., Tkalčić, H., Wölbern, I., Rümpker, G., Bodin, T. & Haugmard, M., 2015. Crustal and uppermost mantle structure variation beneath La Réunion hotspot track, *Geophys. J. Int.,* **203**(1), 107–126.

Grigoli, F., Cesca, S., Dahm, T. & Krieger, L., 2012. A complex linear least-squares method to derive relative and absolute orientations of seismic sensors: orientations of seismic sensors, *Geophys. J. Int.,* **188**(3), 1243–1254.

Hosseini, K., 2015. 'obspyDMT (Version 1.0.0) [software]'. Available at: https://github.com/kasra-hosseini/obspyDMT, last accessed 7 April 2015.

Kennett, B.N. & Engdahl, E.R., 1991. Traveltimes for global earthquake location and phase identification, *Geophys. J. Int.,* **105**(2), 429–465.

Laske, G., 1995. Global observation of off-great-circle propagation of long-period surface waves, *Geophys. J. Int.,* **123**(1), 245–259.

Mainprice, D., 2015. *Seismic Anisotropy of the Deep Earth from a Mineral and Rock Physics Perspective, in Treatise on Geophysics,* pp. 487–538, Elsevier.

Niu, F. & Li, J., 2011. Component azimuths of the CEArray stations estimated from *P*-wave particle motion, *Earthq. Sci.,* **24**(1), 3–13.

Pettersen, Ø. & Maupin, V., 2002. Lithospheric anisotropy on the Kerguelen hotspot track inferred from Rayleigh wave polarisation anomalies, *Geophys. J. Int.,* **149,** 225–246.

Reymond, D., 2010. Différentes approches pour une estimation rapide des paramètres de source sismique: application pour l'alerte aux tsunamis, *Doctorat Thesis,* Université de Polynésie Française, Tahiti.

Rossum, G., 1995. *Python Reference Manual,* CWI (Centre for Mathematics and Computer Science).

Rousseeuw, P.J. & Croux, C., 1993. Alternatives to the median absolute deviation, *J. Am. Stat. Assoc.,* **88**(424), 1273–1283.

Rueda, J. & Mezcua, J., 2015. Orientation analysis of the Spanish broadband national network using Rayleigh-wave polarization, *Seismol. Res. Lett.,* **86**(3), 929–940.

Scheingraber, C., Hosseini, K., Barsch, R. & Sigloch, K., 2013. ObsPyLoad: a tool for fully automated retrieval of seismological waveform data, *Seismol. Res. Lett.,* **84**(3), 525–531.

Schimmel, M. & Gallart, J., 2004. Degree of polarization filter for frequency-dependent signal enhancement through noise suppression, *Bull. seism. Soc. Am.,* **94**(3), 1016–1035.

Schimmel, M., Stutzmann, E., Ardhuin, F. & Gallart, J., 2011. Polarized Earth's ambient microseismic noise, *Geochem. Geophys. Geosyst.,* **12**(7), doi:10.1029/2011GC003661.

Schlindwein, V. & Schmid, F., 2016. Mid-ocean-ridge seismicity reveals extreme types of ocean lithosphere, *Nature,* **535**(7611), 276–279.

Scholz, J.-R., 2014. Local seismicity of the segment-8 volcano at the ultraslow spreading Southwest Indian Ridge, *Master Thesis,* Technische Universität Dresden, Dresden.

Schulte-Pelkum, V., Masters, G. & Shearer, P.M., 2001. Upper mantle anisotropy from long-period P polarization, *J. geophys. Res.,* **106**(B10), 21 917–21 934.

Sigloch, K., 2013. Short Cruise Report METEOR Cruise 101, 1–9, doi:10.2312/CR_M101.

Stachnik, J.C., Sheehan, A.F., Zietlow, D.W., Yang, Z., Collins, J. & Ferris, A., 2012. Determination of New Zealand Ocean Bottom Seismometer Orientation via Rayleigh-wave polarization, *Seismol. Res. Lett.,* **83**(4), 704–713.

Stähler, S.C. *et al.*, 2016. Performance report of the RHUM-RUM ocean bottom seismometer network around La Réunion, western Indian Ocean, *Adv. Geosci.,* **41,** 43–63.

Wang, X., Chen, Q., Li, J. & Wei, S., 2016. Seismic sensor misorientation measurement using *P*-wave particle motion: an application to the NECsaids array, *Seismol. Res. Lett.,* **87**(4), 901–911.

Webb, S.C., 1998. Broadband seismology and noise under the ocean, *Rev. Geophys.,* **36**(1), 105–142.
Wessel, P., Smith, W.H., Scharroo, R., Luis, J. & Wobbe, F., 2013. Generic mapping tools: improved version released, *EOS, Trans. Am. geophys. Un.,* **94**(45), 409–410.
Whittaker, J.M., Goncharov, A., Williams, S.E., Müller, R.D. & Leitchenkov, G., 2013. Global sediment thickness data set updated for the Australian-Antarctic Southern Ocean: Technical Brief, *Geochem. Geophys. Geosyst.,* **14**(8), 3297–3305.
Williams, T. & Kelley, C., 2015. Gnuplot 5.0—an interactive plotting program, last accessed 7 June 2015.
Young, P., 2015. *Everything You Wanted to Know About Data Analysis and Fitting But Were Afraid to Ask,* Springer.
Zha, Y., Webb, S.C. & Menke, W., 2013. Determining the orientations of ocean bottom seismometers using ambient noise correlation, *Geophys. Res. Lett.,* **40**(14), 3585–3590.

SUPPORTING INFORMATION

Supplementary data are available at *GJIRAS* online.

Table summarizing the RHUM-RUM OBS locations and characteristics.
List of individual P-pol and R-pol measurements used to *orient* the OBS.
Detailed version of data problems recognized by orienting the OBS.
Figure A. Component labelling after raw-to-seed data conversion (INSU-IPGP right-handed system; DEPAS/GEOMAR left-handed system), and convention as defined by GSN (Global Seismographic Network) (left-handed system).
Figure B. Individual R-pol orientation measurements for DEPAS station RR10, based on swapped horizontal components (top) and correctly assigned horizontal components (bottom). One obtains many more measurements in the correct case. For 'C1' data culling, refer to paper.
Figure C. Individual R-pol orientation measurements for INSU-IPGP station RR29, based on swapped horizontal components (top) and correctly assigned horizontal components (bottom). One obtains many more measurements in the correct case. For 'C1' data culling, refer to paper.
Figure D. Individual P-pol (top) and R-pol (bottom) orientation measurements for GEOMAR station RR53 with components '1' and 'Z' being swapped (GSN frame). Each method delivers a self-consistent average OBS orientation (for P-pol more scattering is observed, but could be reasonably explained by lower signal-to-noise ratios), however, comparing the two methods suggests a 180° discrepancy, induced by a *P*-waveform polarity inversion. Checking the P-pol measurements for this 180° ambiguity, we found unsolvable contradictions of waveform polarities in both the horizontal and vertical components, suggesting a severe data problem.
Figure E. Individual P-pol (top) and R-pol (bottom) orientation measurements for GEOMAR station RR53 with correctly assigned components. Compared to the swapped case (Fig. D), we find P-pol and R-pol to deliver many more individual measurements that scatter less, and averaged OBS orientations of good agreement. No 180° ambiguity contradictions for the *P*-waves remain.
Figure F. R-pol OBS orientations estimates (dots) obtained for noisy GEOMAR station RR33 (top) and good-quality INSU-IPGP station RR29 (bottom). Measurements are shown in dependence of *counts*, and were defined as 'individual' and thus retained, if *counts* $\geq$ 7000 (vertical black line, see paper). For both stations, we found an ample amount of measurements that do not pass that criterion; these rejected measurements show no convergence of orientations for noisy RR33, but a clear convergence for good quality station RR29, suggesting a significant higher noise level at RR33. For RR29, an accurate OBS orientation can be averaged for measurements with *counts* $\geq$ 7000. Dot colours refer to earthquake depths and show that they had no significant influence on our statistics.
Table S1. Station information for all 57 free-fall ocean-bottom seismometers (OBSs) used in the RHUM-RUM project. 13 stations did not record (red boxes), and 4 stations were too noisy to estimate sensor orientations using either *P*-wave or Rayleigh wave polarizations (orange boxes) (Stähler *et al*. 2016). Abbreviation "gz" in the status column refers to the "glitch" on the vertical component of INSU-IPGP seismograms. The "glitch" is a characteristic, complex pulse shape of roughly 1200 s duration occurring every 3620 s (Stähler *et al*. 2016). They did not affect our orientation measurements, but are mentioned for completeness only. OBS types: DEPAS and GEOMAR are of the LOBSTER type, INSU-IPGP are of the LCPO2000-BBOBS type. For details on station failures, noise levels, OBS types and data records, see Stähler *et al*. (2016).